Internal Tide Generation over Topography: Experiments with a Free-Surface *z*-Level Ocean Model

YOUYU LU

Department of Oceanography, Dalhousie University, Halifax, Nova Scotia, Canada

DANIEL G. WRIGHT

Bedford Institute of Oceanography, Fisheries and Oceans Canada, Dartmouth, Nova Scotia, Canada

DAVID BRICKMAN

Bedford Institute of Oceanography, Fisheries and Oceans Canada, Dartmouth, Nova Scotia, Canada

ABSTRACT

A three-dimensional, *z*-level, primitive-equation ocean circulation model (DieCAST) is modified to include a free-surface and partial cells. The updating of free-surface elevation is implicit in time so that the extra computational cost is minimal compared with the original DieCAST code, which uses the rigid-lid approximation. The addition of partial cells allows the bottom cell of the model to have variable thickness, hence improving the ability to accurately represent topographic variations. The modified model is tested by solving a two-dimensional, linearized problem of internal tide generation over topography. Baines' method is modified to more cleanly separate the internal tide from the full solution. The model results compare favorably with the semianalytic solution of Craig. In particular, the model reproduces the predicted variation of internal tide energy flux as a function of the ratio of bottom slope to characteristic slope.

1. Introduction

DieCAST is a finite-difference numerical model that solves the three-dimensional primitive equations governing the ocean circulation. It is a *z*-level model, that is, the vertical space is discretized into cells that do not vary in thickness over the horizontal. The original code includes the rigid-lid approximation with the surface pressure updated by solving a two-dimensional (2D) elliptic equation. The DieCAST model has been successfully applied to simulate the circulation in oceans and lakes driven by wind, buoyancy flux, and boundary mixing (e.g., Dietrich and Lin 1994; Davidson et al. 1998; Sheng et al. 1998; and Sheng 2001, hereafter SHE).

Two limiting features of the model are 1) the exclusion of surface gravity waves by the rigid-lid approximation and 2) the use of fixed *z* levels in the vertical discretization, potentially causing a poor representation of topographic variations. The first weakness particu-larly limits the application of the model in coastal waters if one wants to simulate motions driven by tides and synoptic atmospheric forcings. To overcome this weakness, the surface elevation must be free to change in response to divergence and convergence of the depth-integrated flow. Various schemes have been proposed for incorporating a free-surface into general circulation models. In this study, we choose to implement the time-implicit scheme of Dukowicz and Smith (1994) rather than an explicit scheme such as that considered by Killworth et al. (1991). This choice is motivated by the desire to avoid major changes to the code while retaining the computational efficiency of the rigid-lid model. Both goals are achieved satisfactorily using Dukowicz and Smith's (1994) method.

With fixed-height *z* levels, topographic changes such as a continental slope are represented by a staircase approximation. Obviously, the accuracy of this approx-imation increases with an increase in the number of levels and a decrease in the thickness of the levels, hence, an increase in computational cost. By contrast, terrain-following coordinates (e.g., the σ coordinate) can accurately resolve topographic changes even with a single layer. To minimize this weakness, we use the method of partial cells (Adcroft et al. 1997; Pacanowski

Corresponding author address: Dr. Youyu Lu, Physical Ocean-ography Research Division, Scripps Institution of Oceanography, University of California, San Diego, 9500 Gilman Drive, La Jolla, CA 92093-0230.
E-mail: youyu@fjord.ucsd.edu

and Gnanadesikan 1998) in which the bottom cell of each vertical column has variable thickness (uniform over each cell) in order to more accurately represent the true water depth. We will show that the use of partial cells significantly improves the model solution above the sloping bottom. Terrain-following coordinates have another advantage, that is, the boundary layer near the sea bed can be better resolved by increasing the number of layers near the bottom. The use of partial cells does not help to resolve the bottom boundary layer over variable topography; however, it does help in situations where topographic variations play an important role, but the topography is not well represented without using an undesirably large number of fixed-height z levels. Advantages of using a z-level model include the convenience of easier analysis of results and the elimination of the pressure gradient error associated with σ-coordinate models when both density stratification and topographic gradients are present (Haney 1991; Mellor et al. 1994).

It should be noted that neither fixed z levels nor σ coordinates are well suited to focusing vertical resolution in the vicinity of the thermocline where shear production of turbulence may be particularly important (e.g., Xing and Davies 1996, 1998). Fixed z levels may have some advantage over σ coordinates for this problem, but isopycnal models are clearly better suited to thermocline problems than either of the other formulations.

The model modifications are tested using an idealized study of internal tide generation over sloping topography. For this problem, terrain-following coordinates have an additional advantage over fixed z-level models that was not mentioned above. In order to accurately represent the internal waves that propagate onto the shelf, at least several layers are required on the shallow side of the slope. Obviously terrain-following coordinates are well suited to handling this problem. In our z-level model, we will choose our vertical grid resolution to be finer near the surface in order to reasonably resolve the vertical structure of the internal wave field on the shelf. It is noteworthy that most previous studies of internal tide generation (e.g., Holloway 1996; Xing and Davies 1998) have been conducted with models using terrain-following coordinates; it is not obvious how fine the horizontal and vertical resolutions of a z-level model will have to be in order to successfully solve this problem.

The internal tide generation problem is particularly relevant to the validation of the model extensions considered here because the surface tide serves as the energy source, and the bottom topography plays an essential role in the barotropic-to-baroclinic energy transfer. Further, the specific problem considered here is appropriate for model validation because results can be readily compared with those from a semianalytic solution documented by Craig (1987).

This modeling study, although idealized, complements previous modeling efforts focused on the internal tide generation problem (e.g., Holloway 1996; Cummins and Oey 1997; Xing and Davies 1998; Holloway and Merrifield 1999). The results of these previous studies reveal that the generation of waves strongly depends on topographic and stratification variations. The wave field undergoes large variations over relatively small spatial scales, consistent with observations. It has long been speculated that the energy transfered from surface to internal tides plays an important role in both coastal and deep ocean mixing (e.g., Sandstrom and Oakey 1995; Munk 1997). On the other hand, there is observational evidence, for example, from satellite altimetry data (Ray and Mitchum 1996), that shows the propagation of internal tides over thousands of kilometers from their source regions. The development and application of models that can deal with this problem and the analysis of the results remain challenging issues in oceanography.

As part of this study, we must separate the internal tide field from the full model solution in order to estimate the energy flux carried by the internal tide. We will discuss the necessary modifications to previously proposed methods (e.g., Baines 1982; Holloway 1986). The remainder of the paper is arranged as follows. In the next section, we introduce the idealized study of internal tide generation and present the method used to separate the internal tide from the full model solution. In section 3, we introduce the DieCAST ocean model and its setup to solve this test case. Appendix A discusses details of the free surface formulation, appendix B gives some model details that are unique to the A-grid formulation, and appendix C discusses details of the partial cell implementation. In section 4, we present the model results in terms of the flow field and energy fluxes and make comparisons with theoretical expectations. A summary and conclusions are presented in section 5.

2. Internal tide generation: A test problem

a. The 2D linear problem

The linear, 2D problem of internal tide generation, solved using a semianalytic method by Craig (1987), is formulated as follows. The 2D model geometry is illustrated in Fig. 1. It consists of deep and shallow regions of uniform depth, separated by a linearly sloping region. The model coordinates are chosen such that the topography varies in the x direction; all gradients in the y direction vanish. The depth of the ocean, measured from the undisturbed surface, is $H(x)$. Under the hydrostatic and Boussinesq approximations, the linearized equations for this problem are
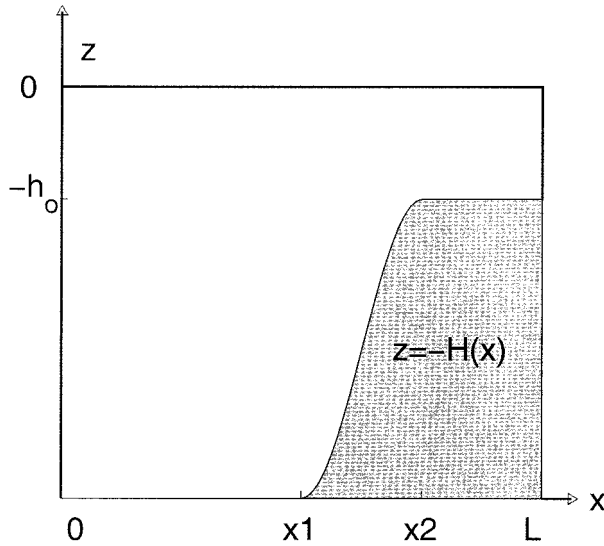
FIG. 1. The model domain, consisting of shallow and deep regions with a sloping bottom in between.

$$u_t - fv + p_x/\rho_* = 0, \qquad (1)$$

$$v_t + fu = 0, \qquad (2)$$

$$p_z + (\rho_o + \tilde{\rho})g = 0, \qquad (3)$$

$$u_x + w_z = 0, \qquad (4)$$

$$\tilde{\rho}_t + w\rho_{oz} = 0, \qquad (5)$$

where the subscripts x and t denote the partial derivatives with respect to the x coordinate and time, respectively; u, v, and w are the x, y, and z velocity components; p is pressure; ρ_* is a reference density (a constant value); $\rho_o(z)$ is the background time-mean density field (chosen to have no horizontal variation); $\tilde{\rho}(x, z, t)$ is the density perturbation due to advection by the tidal flow; and f is the Coriolis parameter.

Because the 2D velocity field is nondivergent, one can define a stream-function ψ such that $u = -\text{Re}\{\psi_z e^{-i\omega t}\}$, $w = \text{Re}\{\psi_x e^{-i\omega t}\}$, where ω is the tidal frequency and $i = \sqrt{-1}$. From (1), (2), (3), and (5), one can derive an equation for ψ:

$$\psi_{xx} - c^2 \psi_{zz} = 0, \qquad (6)$$

where $N = (-g\rho_{oz}/\rho_*)^{1/2}$ is the buoyancy frequency and $c^2 = (\omega^2 - f^2)/N^2$ is the characteristic slope of the internal tide. Craig (1987) seeks the solution for (6) under the following conditions: $\psi = 0$ at $z = -H$ and $\psi_{xx} = 0$ at $z = 0$ (the assumption of an x-independent vertical velocity through $z = 0$ is justified when the x-extent of the model domain is small compared with the wavelength of the surface tide). Craig shows that the solution structure is determined by a nondimensional parameter, $\alpha = H_x/c$, the ratio of bottom slope to the characteristic slope of the internal tide. The value of $\alpha = 1$ divides the problem into subcritical ($\alpha < 1$) and

supercritical ($\alpha > 1$) cases. In the following discussion, we consider the case $f = 0$. However, we note that the solution of (6) for nonzero f can be obtained simply by including the appropriate value of f in the definition of c. The results presented here as a function of α would not be changed for nonzero f, except for the interpretation of α.

b. Separating surface and internal tide components

An internal tide is generated when a barotropic surface tide propagates in stratified water into a region with spatially varying topography. To examine the generation of an internal tide using results from a primitive equation numerical model, one must be able to separate the internal tide field from the full solution.

Following Baines (1982), we first define the ''surface tide'' (denoted by a superscript ''s'') as the solution of the following equations:

$$u_t^s + p_x^s/\rho_* = 0, \qquad (7)$$

$$p_z^s + \rho_o g = 0, \qquad (8)$$

$$u_x^s + w_z^s = 0. \qquad (9)$$

Note that the surface tide solution is calculated in the absence of horizontal density gradients. Baines uses this solution as an estimate of the external mode and subtracts it from the full solution to estimate the internal tide. Following this procedure, we find that the resulting estimate of the baroclinic energy flux exhibits large amplitude periodic variations in x over the flat regions (see Fig. 6a). These anomalous periodic variations indicate that the baroclinic mode is not cleanly separated from the external mode using this method.

We observe that in the presence of background density stratification, $\rho_o(z)$, the isopycnals are heaved by the vertical velocity associated with the surface tide even in the absence of internal wave motion. This results in changes of density and pressure, denoted as $\hat{\rho}$ and $\hat{p}$, respectively, which satisfy

$$\hat{\rho}_t + w^s \rho_{oz} = 0, \qquad (10)$$

$$\hat{p}_z + (\rho_o + \hat{\rho})g = 0; \qquad \hat{p} = p^s \quad \text{at } z = 0. \quad (11)$$

Note that advection by w^s alone determines $\hat{\rho}$ and $\hat{p}$; advection by baroclinic flow is excluded. Clearly, $\hat{\rho}$ and $\hat{p}$ are part of the external mode of response and should be accounted for in the estimation of the surface tide.

The internal tide fields (denoted by a superscript ''i'') are now estimated by

$$(u^i, w^i) = (u - u^s, w - w^s), \qquad (12)$$

$$(p^i, \rho^i) = (p - \hat{p}, \tilde{\rho} - \hat{\rho}), \qquad (13)$$

which satisfy the following equations:

$$u_t^i + p_x^i/\rho_* = (p^s - \hat{p})_x/\rho_*, \qquad (14)$$

$$p_z^i + \rho^i g = 0; \qquad p^i = p - p^s \quad \text{at } z = 0, \quad (15)$$

$$u_x^i + w_z^i = 0, \qquad (16)$$

$$\rho_t^i + w^i \rho_{oz} = 0. \qquad (17)$$

The above approach to separating out the internal tide is introduced in order to account for the pressure effect associated with the heaving of the density field by the barotropic flow, an effect that was not accounted for in the early work of Baines (1982). An alternative approach to dealing with this issue has been taken, for example, by Holloway (1996) and Holloway and Merrifield (1999). In these studies, p^i is calculated using

$$p_t^i = -\rho_* \int_z^0 w^i N^2 \, dz', \qquad (18)$$

where ω^2 has been neglected compared to N^2, consistent with the hydrostatic approximation. With this method, pressure perturbations due to isopycnal heaving by the barotropic tide are excluded from the estimates of p^i. However, the assumption that p^i vanishes at $z = 0$ gives rise to a different error in the estimation of the internal energy flux (see Fig. 5 and the discussion in section 2c).

The term on the right side of (14), $(p_s - \hat{p})_x/\rho_*$, may be thought of as a ''body force'' that generates the internal tide. It is very small over the flat regions (ideally, it should vanish), but its magnitude is amplified over variable topography.

Multiplying (14) by u^i and (15) by w^i and adding, we obtain the kinetic energy budget for the internal tide:

$$[\rho_*(u^i)^2]_t + (u^i p^i)_x + (w^i p^i)_z$$
$$= -g\rho^i w^i + u^i(p^s - \hat{p})_x. \qquad (19)$$

The terms on the left side of (19) are the change of kinetic energy with time and the divergences of horizontal and vertical energy fluxes, respectively. The terms on the right side are the rate of exchange between internal potential energy and internal kinetic energy and the rate of energy transfer from the external to the internal mode.

Similarly, multiplying (17) by $g\rho^i/\rho_{oz}$, we obtain the potential energy equation for the internal tide:

$$\frac{\rho_* N^2}{2}\left[\left(\frac{\rho_i}{\rho_{oz}}\right)^2\right]_t = g\rho^i w^i. \qquad (20)$$

The left side represents the rate of change of internal potential energy, while the term on the right side represents the conversion between internal potential and internal kinetic energy.

Averaging the energy equations over a tidal cycle (denoted by an angle bracket $\langle \, \rangle$), the time-derivative terms drop out, since the tidal forcing is constant, and $\langle g\rho^i w^i \rangle = 0$ because ρ^i and w^i are $90°$ out of phase

according to (17). Hence, the time-averaged energy equation is

$$\langle u^i p^i \rangle_x + \langle w^i p^i \rangle_z = \langle u^i(p^s - \hat{p})_x \rangle, \qquad (21)$$

which represents a balance between the divergence of internal energy flux and the rate of energy conversion from surface to internal tide averaged over a tidal cycle. The right side represents the energy source for the internal tide, and the left side represents the energy redistribution by the internal tide. In section 4, we will show that the energy source is concentrated over the slope as expected and that the baroclinic energy flux over the flat regions is well defined.

The key to the above procedure for separating the internal tide from the full solution lies in determining the pressure field with baroclinic motions eliminated. In the above discussion, this has been achieved by considering the tidal flow that would occur in the absence of density stratification. While this approach gives a reasonable result, one must bear in mind that the energy loss from surface to internal tide is neglected. The potentially significant influence of nonlinear bottom stress is also not considered. The latter effect could be accounted for by using an appropriately linearized bottom stress formulation (e.g., see Wright and Thompson 1983).

One approach that can account for the energy loss to the internal tide is as follows. Consider a supplementary run, which differs from the basic model run by the addition of very strong vertical mixing in the horizontal momentum equations (using an implicit numerical formulation), but with the surface and bottom stress set to zero. By mixing momentum so strongly that baroclinic motions are eliminated over just one or two model time steps, baroclinic motions are effectively eliminated, and the results of this run can be used in place of the results obtained from Eqs. (7)–(11) as an estimate of the ''surface tide.'' The advantage of this approach is that the energy transfer from the surface tide to the internal tide is accounted for, and the pressure variations due to the heaving of the background density field by the surface tide (without any heaving by the baroclinic tide) are automatically determined.

Of course, a disadvantage of both of the approaches discussed above is that a supplementary model run is required to estimate the surface tide so that the baroclinic tide can be obtained by differencing. However, this is a relatively minor price to pay for an improved separation of the surface and internal tidal motions. In the next section, we consider what information about the baroclinic energy flux can be reliably obtained without making any additional runs.

c. Decomposition using only the full model solution

In the previous section, we presented methods for separating the internal tide from the total solution that involved an auxiliary model run in which baroclinic

motion was suppressed. Here we consider whether or not it is possible to separate the energy fluxes associated with the surface and internal tides using only the solution of the full model, which includes the combination of the two tides, without doing an additional model run.

The horizontal velocity associated with the surface tide is usually taken as the depth-average of the full velocity (e.g., Cummins and Oey 1997), that is,

$$u^s = \int_{-H}^{0} u \, dz/H. \tag{22}$$

Once u^s is determined, the vertical velocity associated with the surface tide can be estimated using

$$w^s = (1 + z/H)\eta_t + z/HH_x u^s, \tag{23}$$

where $H_x u^s$ is the vertical velocity just above the bottom associated with u^s. The relative differences between the (u^s, w^s) calculated using (22) and (23) and those obtained by solving (7)–(9) are small. We note that the approximation of u^s by (22) assumes that u^i has a negligible depth-mean ($\int_{-H}^{0} u^i \, dz = 0$), and the determination of w^s by (23) assumes that the contribution $\eta^i = \eta - \eta^s$ [where $\eta^s = p^s/(\rho_* g)$ at $z = 0$ and p^s is determined as in the previous section] to the surface elevation is also negligible. Equations (22) and (23) effectively correspond to making the rigid-lid approximation for the internal tide.

In reality, the surface elevation η^i associated with the internal tide makes a finite contribution to p^i. By separating the surface elevation as $\eta = \eta^s + \eta^i$, the vertical integration of (15) gives

$$p^i = \rho_* g \eta^i + g \int_{z}^{0} \rho^i \, dz'. \tag{24}$$

The second term on the right is well approximated by the approach taken by Holloway (1996). The first term on the right is neglected in Holloway's approach. Neglecting the surface pressure associated with the internal wave field introduces an inaccuracy into the estimation of the vertical structure of the baroclinic energy flux, particularly near the surface. Of course, as the depth increases, the second term becomes increasingly important and can dominate the surface pressure contribution, especially for large-amplitude internal tides.

The depth-integrated energy flux consists of two parts: the part associated with η^i is $\int_{-H}^{0} \rho_* g \langle u^i \eta^i \rangle \, dz$, and that associated with density changes in the interior is $\int_{-H}^{0} g \langle u^i \int_{z}^{0} \rho^i \, dz' \rangle \, dz$. Because the depth-average of u^i is much smaller than the typical magnitude of u^i, the first part is negligible compared with the second part. Consequently, the depth-integrated horizontal energy flux can be calculated from the vertical integral $\int_{-H}^{0} g \langle u^i \int_{z}^{0} \rho^i \, dz' \rangle \, dz$, using the estimates of u^i and ρ^i obtained from (22), (23), and (10)–(13). This is equivalent to calculating p^i using (18), following Holloway (1996). Thus, a reliable estimate of the depth-integrated baro-

clinic energy flux can be obtained from the results of a single run of the full model using either of these two approaches.

3. Model description

a. Model modification

The DieCAST model solves the three-dimensional (3D) nonlinear equations governing temperature, salinity, density, pressure, and velocity. The Boussinesq and hydrostatic approximations are made. The numerical methods used in earlier versions of the DieCAST model are documented by, for example, Dietrich et al. (1987), Dietrich (1992), and Sheng et al. (1998). These papers use the Arakawa C grid for the spatial discretization (e.g., Sheng et al. 1998). In the present study, we work with the A-grid version of DieCAST (see appendix B for some numerical details on the A-grid). The major modifications made to the model code for the purpose of the present work are the additions of a free-surface formulation and allowance for partial thicknesses of the bottom cells of the model. The method used to allow a free surface is the time-implicit scheme suggested by Dukowicz and Smith (1994). Appendix A provides a brief account of how to implement this method in the DieCAST model. The primary advantage of including free-surface effects is that gravity waves associated with the free surface are explicitly represented. The incorporation of partial cells into the DieCAST code is discussed in appendix C. By using this method, a z-level model can accurately resolve the changes in the topography (as with terrain-following coordinates, the accuracy remains limited by horizontal resolution).

b. Model setup

To solve the 2D internal tide generation problem, as outlined in the previous section, we choose the model domain as a straight channel with a single grid in the cross-channel (y) direction and set the velocity, fluxes, and gradients of all quantities to be zero in this direction. In the along-channel (x) direction, the model configuration is identical to that of Craig (1987). The shallow water region is 200 m deep and 50 km wide, the sloping region has a constant slope of 0.01 over a distance of 80 km, and the deep water is 1000 m deep and 500 km wide. The x axis is discretized using uniform grid spacing (Δx). We shall show that the model solutions are sensitive to the choice of Δx. We discretize the vertical space using 25 nonuniformly spaced layers. The thickness of these layers ranges from 20 m near the surface to 69 m near the bottom, with 8 layers in the upper 200 m. As discussed later, such a choice of vertical levels ensures that there is sufficient vertical resolution to resolve the baroclinic mode in both the deep and shallow regions.

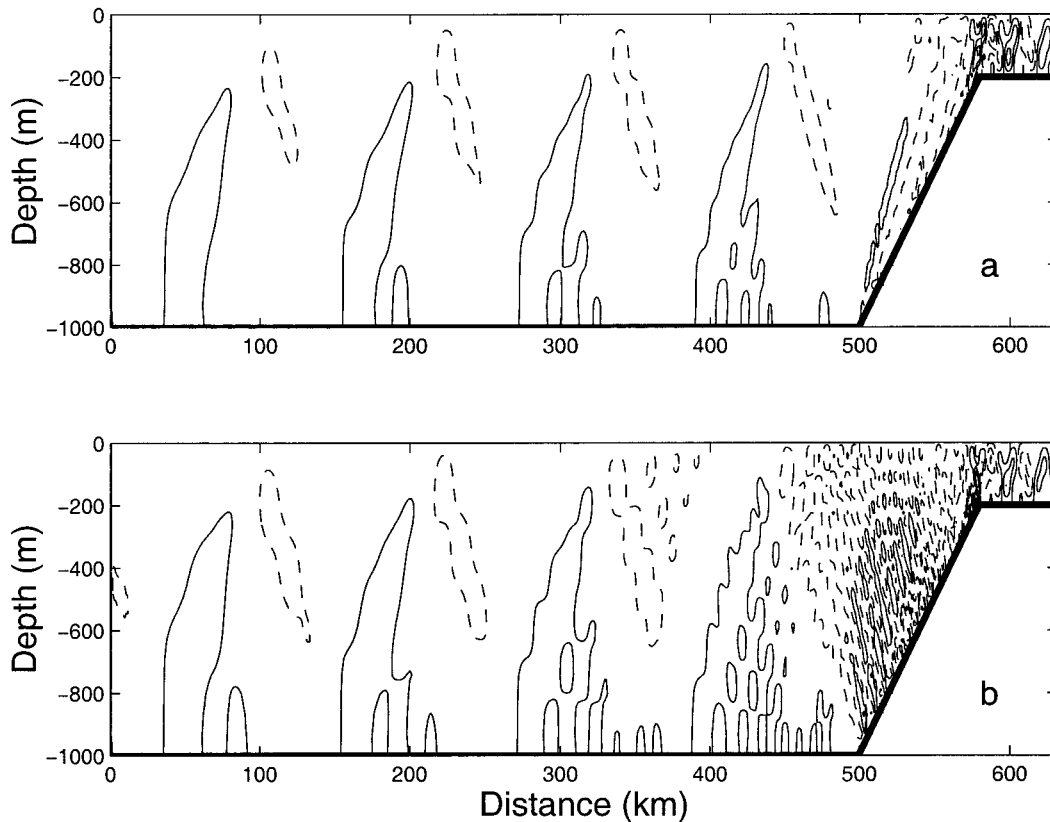At the open boundary in the deep water (at $x = 0$ in

FIG. 2. Snapshots of the vertical velocity in a model run (a) with and (b) without partial cells. Negative values are plotted using broken lines; zero and positive values are plotted using solid lines. The contour interval is 1×10^{-4} m s^{-1}.

Fig. 1) we introduce a surface tide, which propagates into the model domain and sets up a surface elevation of 1 m in magnitude at the coast (at $x = L$ in Fig. 1). The surface tide is reflected at $x = L$ by enforcing zero depth-integrated flow there, but it is allowed to propagate out of the model domain through $x = 0$ using a radiation boundary condition [the radiation phase speed for the surface tide is $(gH)^{1/2}$]. The internal tide is allowed to propagate out through both $x = 0$ and $x = L$ using radiation boundary conditions for the baroclinic mode (the radiation phase speed is taken equal to that of the first baroclinic mode). The tidal frequency is set at $\omega = 10^{-4}$ s^{-1}.

The DieCAST model solves the advection–diffusion equation for temperature and salinity. In this idealized test, we initialize the salinity to be uniform and set zero salt fluxes at all the model boundaries. The salinity fields are thus uniform in both space and time. The density variation is purely due to changes in temperature. The initial temperature field varies linearly in the vertical and is uniform in the horizontal. A linear equation of state is applied, hence the buoyancy frequency (N) is uniform. We run the model with different values of the buoyancy frequency, hence different values of $\alpha = H_x N / \omega$. Insulation conditions for heat are applied at the sur-

face, bottom, and side boundaries. A radiation condition is applied to the temperature at $x = 0$ and $x = L$.

To be consistent with Craig (1987), momentum advection is neglected, heat advection is linearized about the initial state, and minimal subgrid scale mixing is used. No explicit mixing of heat is included in either the horizontal or vertical directions. A slip condition is applied to the velocity at the side boundaries, there is no explicit mixing of momentum in the vertical, and the bottom stress is set to zero. A Laplacian formulation is used for the horizontal mixing of momentum, with the diffusion coefficient set to 10 m^2 s^{-1} (momentum diffusion over a horizontal distance of 3 km requires approximately 9 days, comparable with the maximum time required for the internal waves generated at the sloping topography to propagate out of the model domain).

4. Model results: Validation

a. Internal tide flow fields

We first illustrate the improvement in the model solution achieved by using partial cells. Figure 2 shows two snapshots of the vertical velocity field obtained from simulations with and without partial cells. When
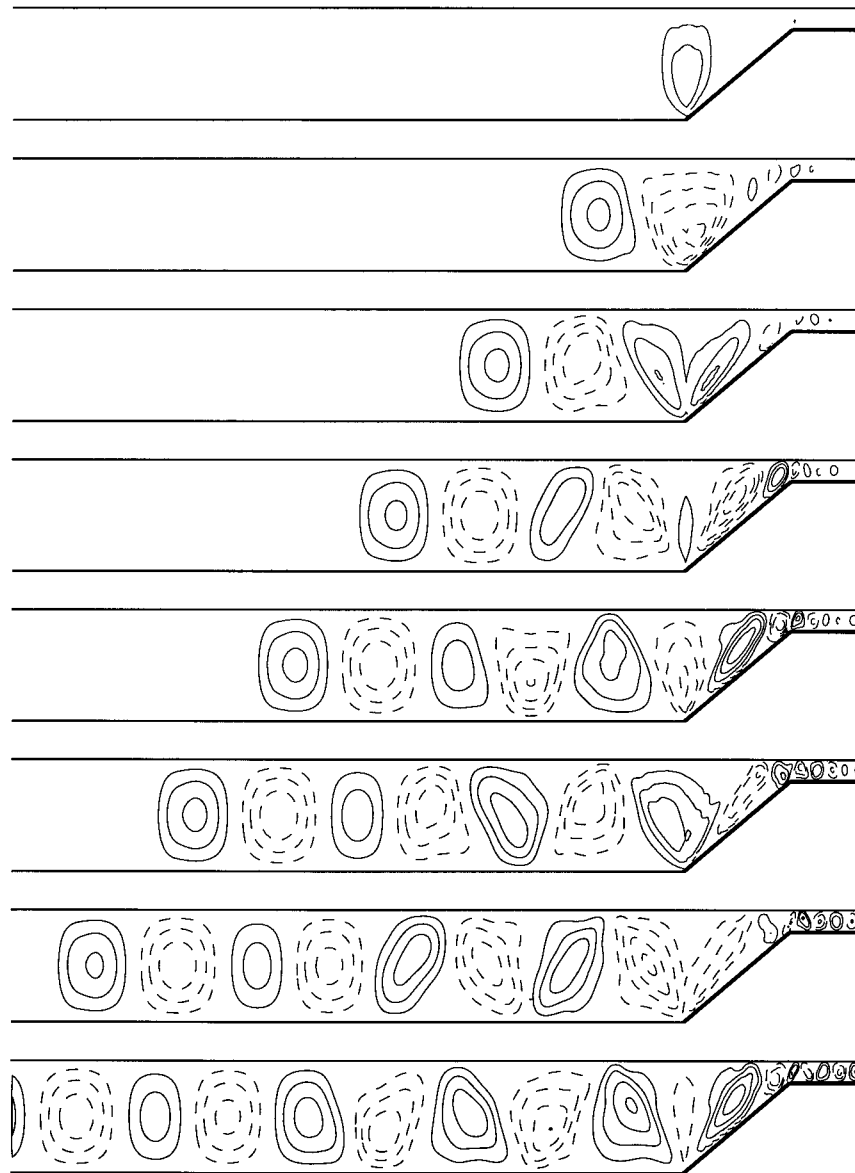
FIG. 3. A time sequence of internal tide streamfunction (ψ^i) plots. Starting from the second panel from the top, each panel lags the one above it by 10.9 (the tidal period is 17.45 h). Negative ψ^i (broken lines) correspond to counterclockwise baroclinic circulation. Positive ψ^i (solid lines) correspond to clockwise circulation. The contour interval is 0.25 m² s⁻¹. The results are for α = 0.6 and were simulated using Δx = 1 km.

only standard vertical cells are used, the poor representation of the sloping bottom leads to substantial grid-scale noise in the velocity field. The noise is not limited over the slope, since the vertical motion generates internal waves that propagate into the flat regions. When partial cells are used, the grid-scale noise is almost completely eliminated, and a smoothly varying velocity field is obtained. The improvements are also evident in the results for other variables and the subsequent calculation of energy fluxes.

The implementation of partial cells has also been validated against the analytic solution of Rhines (1975) for a bottom-intensified Rossby wave in a stratified re-entrant channel. This test of partial cells has been examined previously for an implementation in the GFDL Modular Ocean Model (Pacanowski and Gnanadesikan 1998). Although this test case serves as an additional validation of the model, the results obtained with our implementation of partial cells in the DieCAST model are similar to those presented by Pacanowski and Gnanadesikan and will not be reproduced here. Partial cells are used throughout the rest of the model experiments presented here.
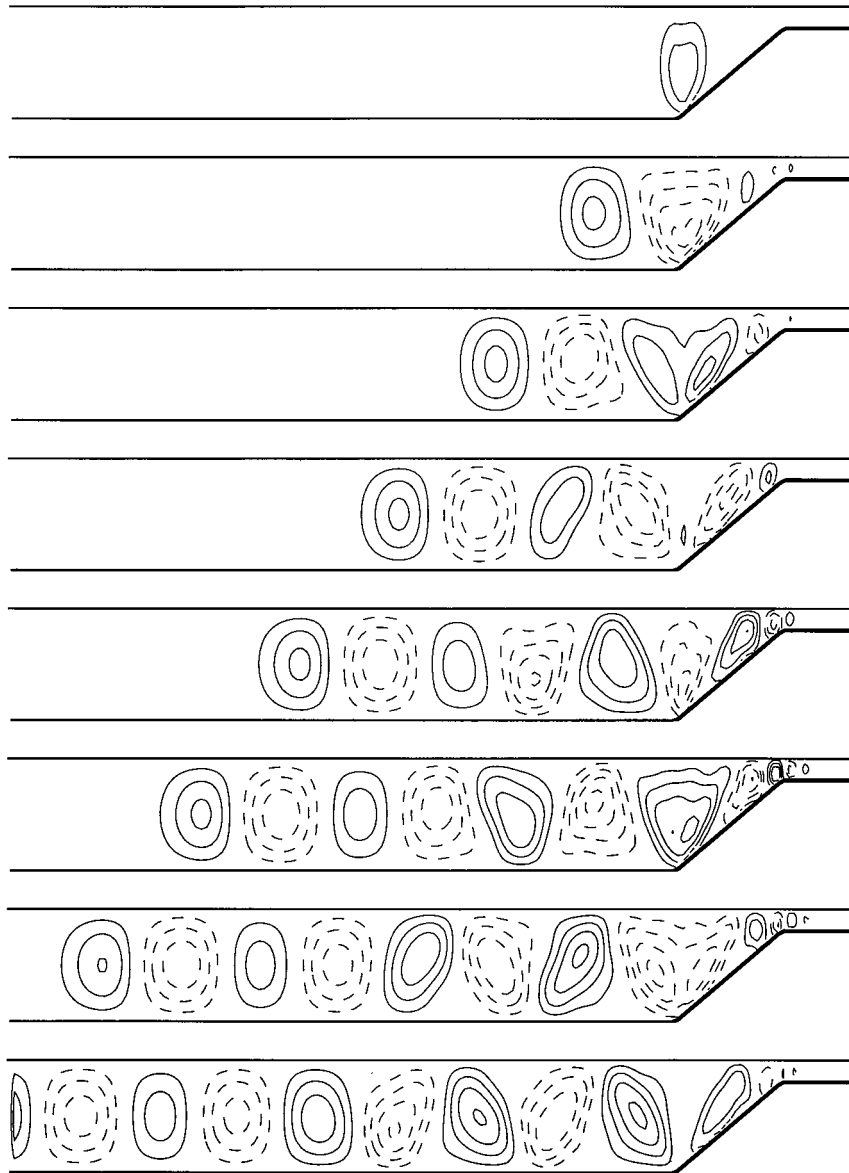
Figure 3 shows a time sequence of streamfunction ψ^i

Fig. 4. Same as in Fig. 3 but with $\Delta x = 4$ km. Note the weaker baroclinic velocity in shallow water.

plots for the internal tide. We define ψ^i such that $u^i = -\psi^i_z$, $w^i = \psi^i_x$ with $\psi^i = 0$ at $z = -H$. The results shown in Fig. 3 are for the subcritical case $\alpha = 0.6$, obtained using a horizontal grid spacing of $\Delta x = 1$ km. The time sequence of ψ^i clearly shows that the internal tide is predominantly generated at the bottom of the slope, after the surface tide arrives there, and propagates toward both the deep ocean and the shelf. The propagation speed is approximately equal to the local phase speed of the first baroclinic mode. After the solution reaches a periodic state, the evolution of ψ^i over a tidal cycle (not shown here) agrees, both qualitatively and quantitatively, with the semianalytic solution of Craig (1987; see his Fig. 5).

It is of interest to consider whether we can achieve similar results to those presented in Fig. 3 with coarser resolution. For $\alpha = 0.6$, we have considered $\Delta x = 2$ km and $\Delta x = 4$ km. Results show that the solution with $\Delta x = 2$ km is very close to that with $\Delta x = 1$ km. For $\Delta x = 4$ km (Fig. 4), the solution does not change significantly in the deep water, but the internal tide in the shallow region is greatly reduced. These conclusions based on idealized experiments are generally consistent with results obtained in much more realistic 3D configurations (e.g., Cummins and Oey 1997; Xing and Davies 1996, 1998).

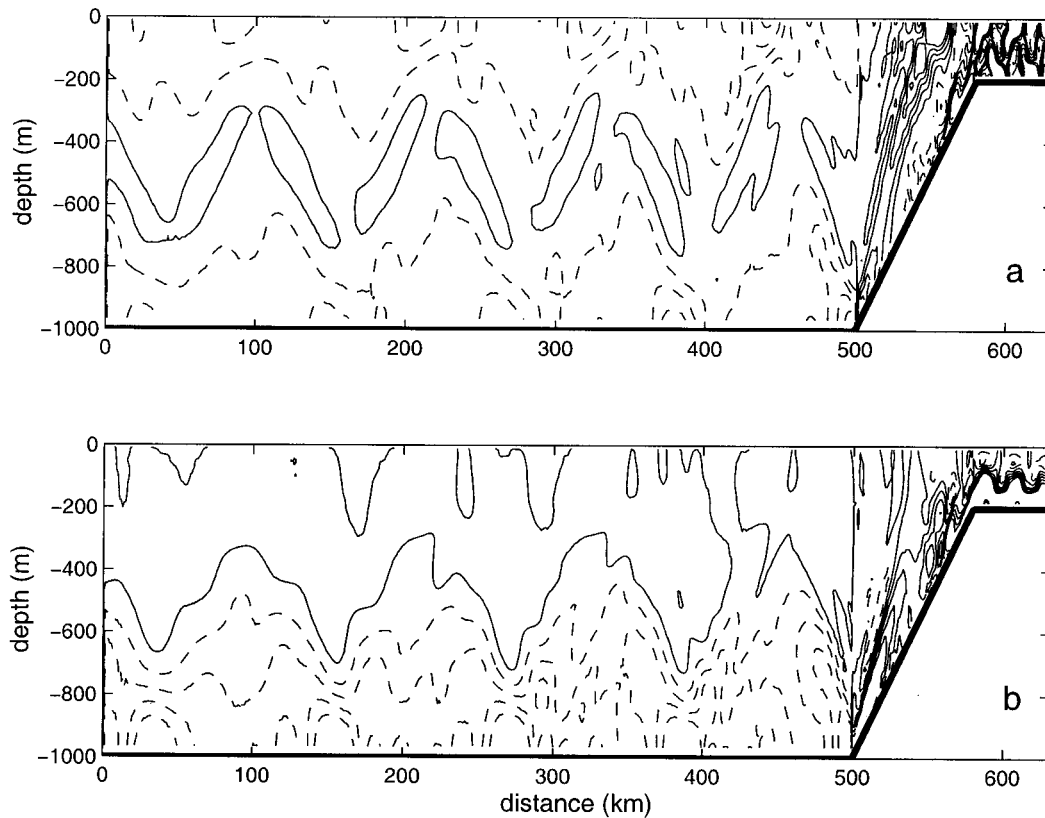The spatial resolution required to accurately reproduce the nature of the internal wave field is related to

FIG. 5. (a) The horizontal energy flux of the internal tide, $\langle u^i p^i \rangle$, for $\alpha = 0.6$. Zero and positive values are plotted as solid lines. Negative values are plotted as broken lines. The contour interval is 0.005 W m^{-2}. (b) Same as (a) except for contour of $\langle u^i \int_z^0 \rho^i \, dz' \rangle$.

the wavelength of the internal tide. In the vertical direction, the wavelength of the first mode equals twice the water depth (for this constant N case), hence 25 levels in deep water and 8 levels in shallow water are adequate to resolve the vertical variations associated with the first internal mode and marginally adequate to resolve the vertical variations in the second mode. For a given characteristic slope, $c = \omega/N$, the horizontal wavelength of the first baroclinic mode is $2H/c = 2\alpha H/H_x$. For $\alpha = 0.6$ and $H_x = 0.01$, the wavelength is 120 km in deep water ($H = 1000$ m) and 24 km in shallow water ($H = 200$ m). Hence $\Delta x = 4$ km is easily sufficient to resolve the internal tide in the deep water but marginal at best in the shallow water. The situation is exacerbated if higher modes are involved in the energy transfers over the slope. For larger α values, the spatial resolution is less of a constraint in the flat regions but more of a constraint over the sloping region.

b. The energy budget

In Fig. 5a, we show the contour lines of the horizontal energy flux, $\langle u^i p^i \rangle$, for $\alpha = 0.6$. In the deep water, the energy flux is directed to the left (negative values). In the shallow water, the flux is directed to the right (positive values). We noted earlier that the pressure p^i as-

sociated with the internal tide includes a contribution from η^i, the sea level change associated with the internal tide [Eq. (24)]. While this contribution is tiny compared with η^s, the influence on the estimation of the baroclinic energy flux is significant. This point is emphasized by Fig. 5b, which shows the quantity $\langle u^i g \int_z^0 \rho^i \, dz' \rangle$, obtained by neglecting η^i in the calculation of the energy flux shown in Fig. 5a. This is effectively equivalent to the result that would be obtained using the approach of Holloway (1996). As noted earlier, the fact that the depth integral of u^i is small results in negligible contribution from η^i to the depth-integrated energy flux (Fig. 6a). However, if one wishes to examine the depth distribution of the internal energy flux, the surface pressure variation associated with the internal tide should be accounted for unless one is confident that the internal tide does not extend to the surface.

Note that if the density variations associated with heaving of the density field by the surface tide are not removed from ρ^i (and hence also from p^i), then the depth-integrated energy flux would include large amplitude variations over the length scale of the internal tide. This erroneous result is shown as the thinner broken line in Fig. 6a. Such variations are a clear indication of poor separation between the surface and internal wave modes.
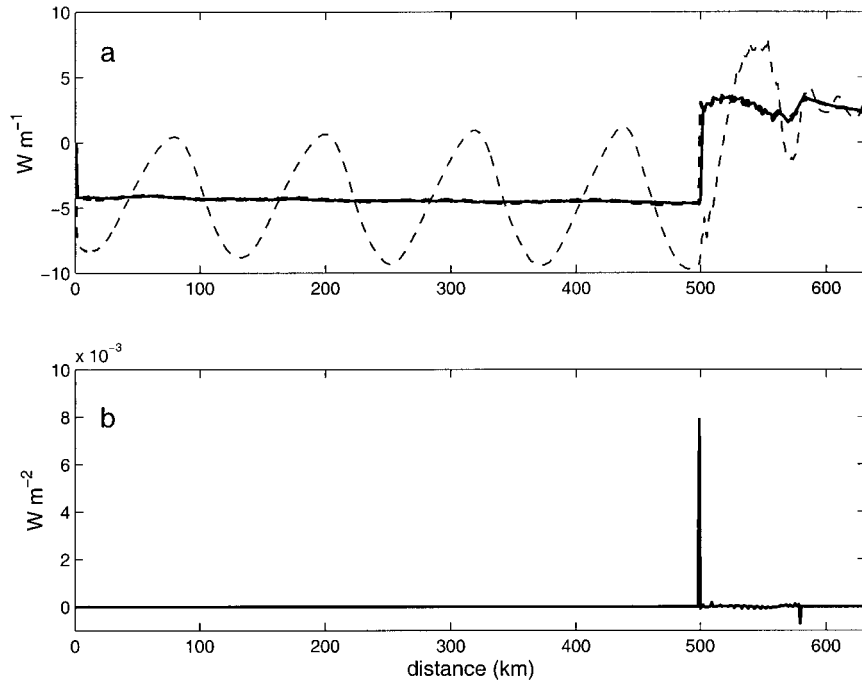
FIG. 6. (a) The depth-integrated horizontal energy fluxes calculated using $\langle u^i p^i \rangle$ (solid line) and $\langle u^i \int_z^0 \rho^i \, dz' \rangle$ (thicker broken line, essentially overlying the solid line). The thinner broken line shows the erroneous result that is obtained when heaving of the density field is not accounted for in the estimation of the pressure variations associated with the surface tide. (b) The depth-integrated values of $\langle u^i (p^s - \hat{p})_x \rangle$, the rate of energy conversion from surface to internal tides. Both (a) and (b) are for the case $\alpha = 0.6$.

Figure 6a shows that the values of the depth-integrated internal tide energy flux jumps from negative to positive at the bottom of the slope. This flux divergence is balanced by the source term $\langle u^i (p^s - \hat{p})_x \rangle$, the conversion rate from surface to internal tidal energy. In Fig. 6b, we plot the depth-integrated values of $\langle u^i (p^s - \hat{p})_x \rangle$. This plot shows that the energy conversion takes place mainly at the bottom of the slope.

The other region with nonzero $\langle u^i (p^s - \hat{p})_x \rangle$ is at the top of the slope where the depth-integrated conversion rate is negative for this geometry and choice of parameters.

Except near the bottom and the top of the slope, the magnitude of $\langle u^i (p^s - \hat{p})_x \rangle$ is small, and the energy fluxes ($\langle u^i p^i \rangle$, $\langle w^i p^i \rangle$) have almost no divergence. Consequently, one can define a scaler Ψ such that $\langle u^i p^i \rangle = -\Psi_z$, $\langle w^i p^i \rangle = \Psi_x$, and Ψ can be used to illustrate the pathway of the baroclinic energy flux, as shown in Fig. 7. The directions of the flux vectors ($\langle u^i p^i \rangle$, $\langle w^i p^i \rangle$) are parallel to the contour lines. Starting from the bottom of the slope, internal tide energy propagates toward the deep water along "rays" that bounce back and forth between sea surface and sea bed. Similar rays also propagate up the slope toward the shallow water.

c. Energy flux as a function of $\alpha = H_x N / \omega$

We now consider the results from a sequence of model runs using different values of α (by changing the background density field ρ_o hence the buoyancy frequency N). The energy fluxes are calculated for each individual run. In Fig. 8, we plot the values of the internal tide energy flux toward the deep ocean [denoted by F_1 as in Craig (1987)] as a function of α. Superimposed on this plot are the values of F_1 calculated by Craig. The agreement between the two sets of values, both in the subcritical ($\alpha < 1$) and supercritical ($\alpha > 1$) regimes, are quite good. An interesting feature of the model calculated values is the presence of two regions of reduced energy flux near $\alpha = 0.4$ and $\alpha = 0.7$. These two anomalies are not indicated by Craig's values (although he did not calculate energy fluxes for as many values of α as presented here). Interestingly, the occurrence of these two reductions of the energy flux approximately coincide with two special cases in terms of internal tide characteristics, as shown in Fig. 9. For the first case, which occurs at $\alpha = 2/3$ for the present model geometry, the wave characteristics link the bottom and top corners of the slope with one reflection at the surface. For the second case, which occurs at $\alpha \approx 0.38$, the wave characteristics link the same two regions with two reflections from the surface. These results are at least qualitatively consistent with the prediction of Müller and Liu (2000) that a linear slope will be transparent to internal waves with this property. [Note that there is a misprint in the sign of the last term in Eq. (39) of Müller and Liu (2000).] In this case, forward-propagating internal waves generated at the base
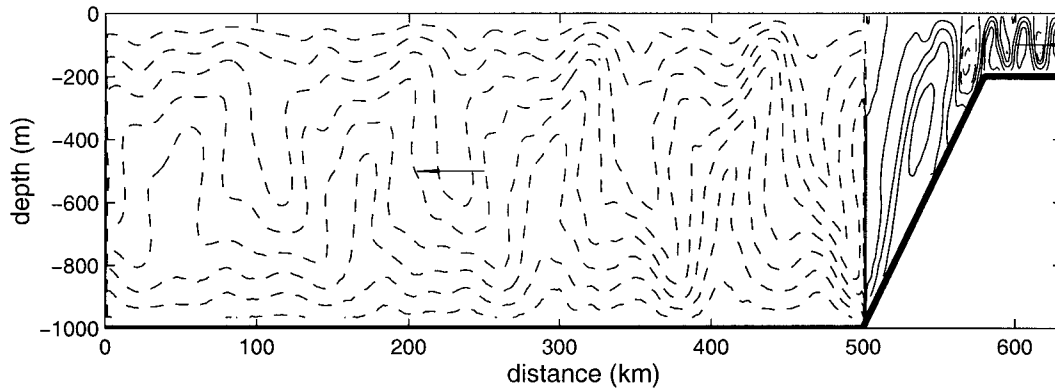
FIG. 7. Contours of Ψ defined as $\langle u^i p^i \rangle = -\Psi_z$, $\langle w^i p^i \rangle = \Psi_x$, for $\alpha = 0.6$. Negative values are plotted as broken lines with a contour interval of 0.5 W m^{-1}. Zero and positive values are plotted as solid lines with a contour interval of 1 W m^{-1}. The vectorial direction of the internal tide energy flux ($\langle u^i p^i \rangle$, $\langle w^i p^i \rangle$) is parallel to the contour lines. The two arrows indicate the directions of the depth-integrated energy fluxes in the deep and shallow waters, respectively.

of the slope should traverse the slope without reflection, resulting in reduced total reflected internal wave energy. The spreading of the anomalies in the α axis is probably influenced by a combination of nonzero diffusion in our model and the approximate representation of the bottom topography by the finite model resolution. Regarding the influence of finite model resolution, it is noteworthy that analytic solutions have singularities at sharp corners (Sandstrom 1976).

5. Conclusions

The addition of a free-surface and partial cells makes two important modifications to the DieCAST ocean circulation model. The time-implicit, free-surface scheme of Dukowicz and Smith (1994) is similar to the implicit method of updating the surface pressure field in the rigid-lid DieCAST model (appendix A). Hence, the

amount of work required to modify the rigid-lid code and the extra computational cost of including a free-surface are minimal. We note that the same free-surface method has been implemented in the Los Alamos Parallel Ocean Program (Smith et al. 1992). The method of including partial cells is that of Adcroft et al. (1997), and an implementation in the GFDL Modular Ocean Model has been discussed previously by Pacanowski and Gnanadesikan (1998). With a free-surface included, the forcing of the surface tide can be explicitly included. The use of partial cells significantly improves the model solution, compared with using standard, fixed-thickness z levels.

To test these new developments, the modified DieCAST model is applied to simulate the 2D, linear problem of internal tide generation over topography.
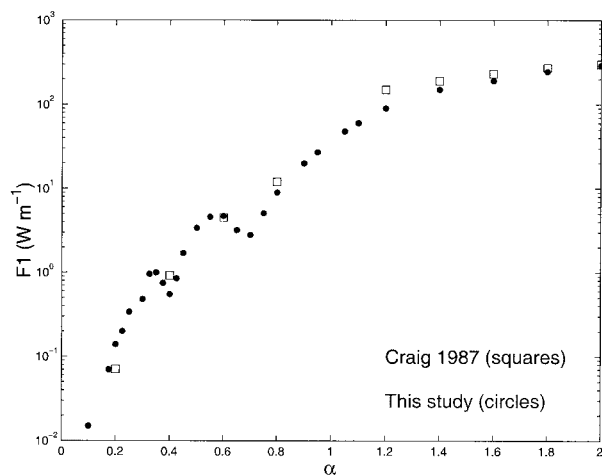

FIG. 8. Magnitude of the internal tide energy flux into the deep ocean as a function of $\alpha = H_x N / \omega$. Squares denote the semianalytical solution of Craig (1987), and solid circles are calculated using the free-surface DieCAST model.
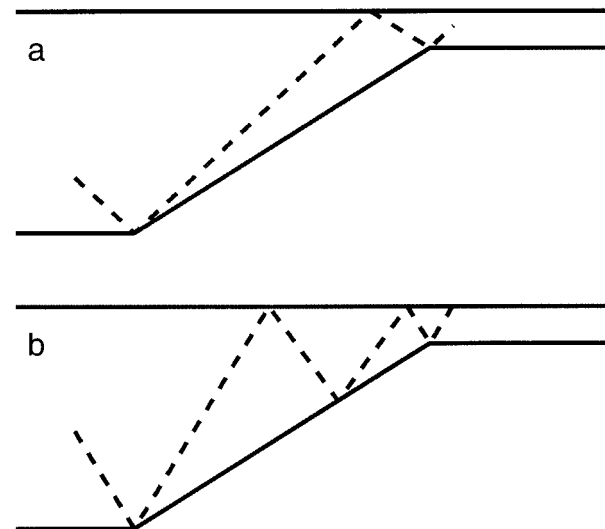

FIG. 9. Internal tide characteristics (broken lines) that link the bottom and top corners of the shelf break. The two cases shown are (a) $\alpha = 2/3$ and (b) $\alpha = 0.38$ for the model geometry specified in section 4a.

The method of separating the internal tide from the full model solution, which includes the motions and density variations associated with the surface tide, is discussed. It is shown that a consistent determination of the energy budget for the internal tide requires accounting for the fact that the density variations due to heaving by the surface tide and the associated pressure variations are part of the external mode and not part of the internal mode. Attention to this point is essential to achieve zero divergence of the depth-integrated internal tide energy flux away from its generation regions. It is also shown that the surface pressure variations associated with the internal tide must be accounted for to accurately esti-mate the vertical structure of the baroclinic energy flux. This latter effect is not critical to the determination of the depth-integrated energy flux associated with the in-ternal tide.

The model is used to determine numerical solutions corresponding to the problem considered by Craig (1987), and results are compared with his semianalytical solution. Close agreement between the numerical model and analytical results are obtained when the spatial res-olution of the model is adequate to resolve the wave-length of the lowest mode. By running the model with different background density gradients, the model pre-dicts a variation of the internal tide energy flux (F_1) as a function of the ratio of bottom slope to characteristic slope (α). The model results reveal two dips in F_1 within the subcritical range of α, but otherwise shows a mono-tonic increase of F_1 with increasing α, in agreement with the results presented by Craig (1987). The two dips in the energy flux occur for the parameter values at which the results of Müller and Liu (2000) predict that a linear slope will be transparent to the internal waves generated at the base of the slope. It is likely that this effect accounts for the reduction in internal wave energy reflected backward from the slope. This question war-rants further investigation but is beyond the scope of the present work.

In summary, the results from this study demonstrate the successful addition of a free-surface and partial cells to a z-level ocean model (DieCAST). The modifications extend the applicability of the model to include prob-lems that require the relaxation of the rigid-lid approx-imation and more accurate representation of topographic changes. The idealized test case of internal tide gen-eration can easily be extended to more general situations that include nonlinear effects, turbulent mixing, and three-dimensionality. Potential problems with previous approaches to separating the surface and internal tides have been identified, and simple corrective measures have been suggested.

APPENDIX A

Implicit Free-Surface Method

To relax the rigid lid approximation, we linearize the kinematic boundary condition at the sea surface to give

$$w = \eta_t, \text{ at } z = 0. \tag{A1}$$

Vertical integration of the nondivergent continuity equa-tion then gives

$$\eta_t + \nabla \cdot \left(\int_{-H}^{0} \mathbf{u} \, dz \right) = 0, \tag{A2}$$

and integration of the hydrostatic equation gives

$$p = \rho_* g \eta + g \int_{z}^{0} \rho \, dz'. \tag{A3}$$

The horizontal momentum equation is

$$\mathbf{u}_t + \mathcal{L}(\mathbf{u}) + \mathbf{f} \times \mathbf{u}$$
$$= -g\nabla \int_{z}^{0} \rho/\rho_* \, dz' - g\nabla\eta + D_m(\mathbf{u})$$
$$+ (A_v \mathbf{u}_z)_z. \tag{A4}$$

In the above equations, we define $\mathbf{u}$ as the horizontal velocity vector; η is the surface elevation measured from the position of the undisturbed sea surface ($z = 0$); $z = -H(x, y)$ is the position of the bottom; $\mathbf{f}$ is an upward directed vector with magnitude equal to the Cor-iolis parameter; (∇, $\mathcal{L}$, D_m) are the horizontal gradient, advection, and horizontal diffusion operators, respec-tively; and A_v is the vertical viscosity.

The implicit time-differencing scheme of Dukowicz and Smith (1994) is applied to discretize (A2) and (A4). This leads to

$$(\eta^{n+1} - \eta^n)/\Delta t + \nabla \cdot \int_{-H}^{0} \bar{\mathbf{u}}^n \, dz = 0, \tag{A5}$$

$$(\mathbf{u}^{n+1} - \mathbf{u}^{n-1})/(2\Delta t) + \mathcal{L}(\mathbf{u}^n) + \mathbf{f} \times \mathbf{u}^n$$
$$= -g\nabla \int_{z}^{0} \rho^n/\rho_* \, dz' - g\nabla\bar{\eta}^n + D_m(\mathbf{u}^{n-1})$$
$$+ (A_v \mathbf{u}_z^{n+1})_z, \tag{A6}$$

where

$$\overline{\mathbf{u}}^n = \theta\mathbf{u}^{n+1} + (1 - \theta)\mathbf{u}^n, \tag{A7}$$

$$\overline{\eta}^n = \alpha_1\delta\eta + (\alpha_1 + \alpha_2)\eta^n + (1 - \alpha_1 - \alpha_2)\eta^{n-1}, \tag{A8}$$

and $\delta\eta = \eta^{n+1} - \eta^n$. The values of θ, α_1, and α_2 determine whether an explicit or implicit scheme is employed to deal with the free surface elevation. $\theta = 1$, $\alpha_1 = 1$, and $\alpha_2 = 0$ give a fully implicit scheme while $\theta = 0.5$, $\alpha_1 = \alpha_2 = 1/3$ give a time-centered explicit scheme. Dukowicz and Smith (1994) give a detailed discussion of the influences of different values of θ and α on the physical and computational modes. They also show that the linear approximation (A1) can be replaced by its nonlinear counterpart, and the vertical integral in (A2) can be performed from $z = -H$ to $z = \eta$. Also, a variable thickness top-layer could be implemented into the DieCAST model following Dukowicz and Smith's formulation. However, the linear formulation is justified when the change of surface elevation is much smaller than the total water depth.

The surface elevation and velocity fields are updated according to the following procedure.

1) The velocity $\mathbf{u}$ is partially updated based on explicit treatment of advection, Coriolis force, the baroclinic pressure gradient, and η at previous time steps as well as horizontal mixing; the trial field obtained is denoted as $\hat{\mathbf{u}}^{n+1}$;
2) the influence of vertical mixing on $\hat{\mathbf{u}}^{n+1}$ is accounted for using an implicit scheme; the new trial field is denoted as $\tilde{\mathbf{u}}^{n+1}$;
3) η is implicitly updated by solving the following elliptic equation for $\mathcal{P} = 2\Delta t\alpha_1 g\delta\eta$:

$$\boldsymbol{\nabla}\cdot(H\boldsymbol{\nabla}\mathcal{P}) - \gamma\mathcal{P} = F + F^*, \tag{A9}$$

where $F = \boldsymbol{\nabla}\cdot\int_{-H}^0 \hat{\mathbf{u}}^{n+1}\,dz$, $F^* = (1/\theta - 1)\boldsymbol{\nabla}\cdot\int_{-H}^0 \mathbf{u}^n\,dz$, and $\gamma = 1/[2(\Delta t)^2 g\alpha_1\theta]$; and
4) the velocity field is finally updated using

$$\mathbf{u}^{n+1} = \hat{\mathbf{u}}^{n+1} + \boldsymbol{\nabla}\mathcal{P}. \tag{A10}$$

When the rigid-lid approximation is made, the position of the surface is fixed at $z = 0$; η_t in (A1) and (A2) is zero, and η in (A3) and (A4) is replaced by $p_o/(\rho_* g)$, where p_o is the pressure under the rigid-lid. In the rigid-lid code, the updating procedure is similar to that described above except for the following changes (cf., Sheng et al. 1998): 1) in step 1), the updating of $\mathbf{u}$ is based on the surface pressure at the previous time step, p_o^n, instead of η^{n-1} and η^n; and 2) the elliptic equation is constructed for $\mathcal{P} = \delta p_o$, and (A9) is replaced by

$$\boldsymbol{\nabla}\cdot(H\boldsymbol{\nabla}\mathcal{P}) = F. \tag{A11}$$

Except for the change of forcing terms, the most significant difference between (A9) and (A11) is the appearance of the $\gamma\mathcal{P}$ term in (A9). Because the value of γ is a constant as long as Δt, θ, and α_1 are fixed, the extra computations required in updating η are negligible.
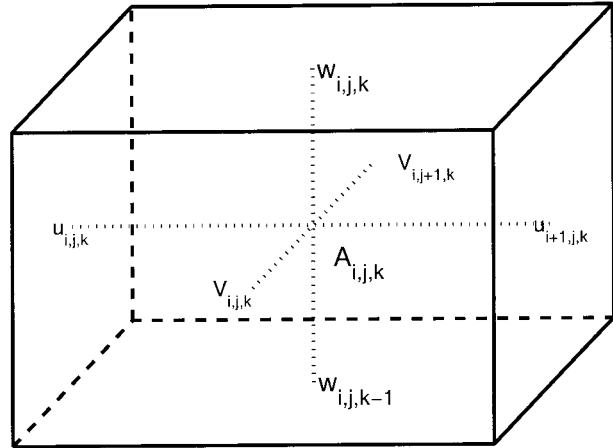
The updating of the temperature (T) and salinity (S)

FIG. B1. A control volume center on $A_{i,j,k}$, where (p, T, S, ρ, u, v)$_{i,j,k}$ are calculated. For the Arakawa A-grid, (p, T, S, ρ, u, v)$_{i,j,k}$ actually represent averages over the cell volume. The positions of the staggered C-grid velocities are denoted by ($U_{i,j,k}$, $V_{i,j,k}$, $w_{i,j,k}$).

fields follows the same procedure as in the rigid-lid model (e.g., Sheng et al. 1998).

APPENDIX B

A-Grid Details

The version of DieCAST used in the present study uses the Arakawa A-grid formulation. It was developed as a modification of the C-grid version of the DieCAST model discussed by Sheng et al. (1998) and has benefited from numerous consultations with Dr. David Dietrich, the developer of the original version of DieCAST. Details of the C-grid version of DieCAST are presented by Sheng et al. and will not be repeated here. We discuss only the differences between the C-grid and the A-grid formulations.

The most important differences between the A-grid and C-grid formulations are associated with the spatial discretization of the horizontal velocity components u and v. On the A-grid, u and v are defined at the center of each cell (i.e., colocated with T, S, ρ, and p), whereas in the C-grid formulation, u and v are defined on the bounding faces of the control volume. Figure B1 shows an isolated control volume centered at an A-grid point. The A-grid point and the locations at which the C-grid velocity components are defined are each indicated. The colocation of u and v on the A-grid overcomes the difficulty with the C-grid in estimating the Coriolis terms. However, the use of a control volume approach requires knowledge of the velocity components normal to the faces of the model grid cells, that is, at the C-grid locations. Thus interpolations of the horizontal velocity components from the A-grid to the C-grid locations are required.

As discussed in appendix A, a trial velocity $\hat{\mathbf{u}}^{n+1}$ is first determined at the A-grid points, which includes all effects except for a corrective step to ensure continuity.

The correction for continuity is done on the C-grid ve-
locity components, and the required velocity adjust-
ments are then interpolated to the A-grid. The first step
in this procedure is to interpolate the trial velocity $\hat{\mathbf{u}}^{n+1}$
from A-grid points to the C-grid cell surfaces. To do
this, we use a straightforward, level by level, linear
interpolation in the horizontal (the adjustment required
for partial cells is discussed in appendix C). The depth-
integrated velocity, or transport, at the C-grid locations
is then calculated, and F, the term on the right side of
(A9), is obtained. After solving (A9), the C-grid veloc-
ities are adjusted to be consistent with the modification
of the surface pressure gradient. After this adjustment,
the C-grid transport satisfies the depth-integrated con-
tinuity equation. The vertical velocity (w) is determined
at the z levels between the levels where T, S, u, and v
are defined by integrating the divergence equation ex-
pressing incompressibility. This yields a nondivergent
velocity field which, in general, is subsequently used in
a control volume treatment of the advective terms for
heat, salt, and momentum. For the linearized problem
considered here, only heat advection is considered.

Once the velocity has been corrected to satisfy the
continuity equation on the C-grid, the changes required
by this correction are interpolated back to the A-grid.
Since these changes are associated entirely with a
change in the surface pressure gradient, the velocity
changes on the A-grid are taken to be depth-independent
and determined by interpolating the depth-integrated
transports from the C-grid to the A-grid. This completes
the updating of the velocity on both the A- and C-grids.

One other interpolation is required by the A-grid for-
mulation. Since the velocity is updated on the A-grid
but the pressure gradient is most naturally determined
at the C-grid locations, the pressure gradient must be
interpolated from the C-grid to the A-grid. To do this,
we use simple linear interpolation with the normal com-
ponent of the pressure gradient set to zero at all solid
boundaries. The justification for the latter choice is sim-
ple. It is equivalent to determining the changes in the
C-grid velocity associated with the pressure gradient and
then linearly interpolating from the C-grid to the A-
grid.

APPENDIX C

Partial Cells: Improving the Representation of Topography

A detailed discussion of the implementation of partial
cells in the B-grid GFDL MOM2 model is given by
Pacanowski and Gnanadesikan (1998). Although we use
an A-grid version of DieCAST, making some algebraic
and numerical details different, the basic considerations
of the two implementations are the same. Here we brief-
ly review the changes in the model code that are required
when adding partial cells and refer readers to Paca-
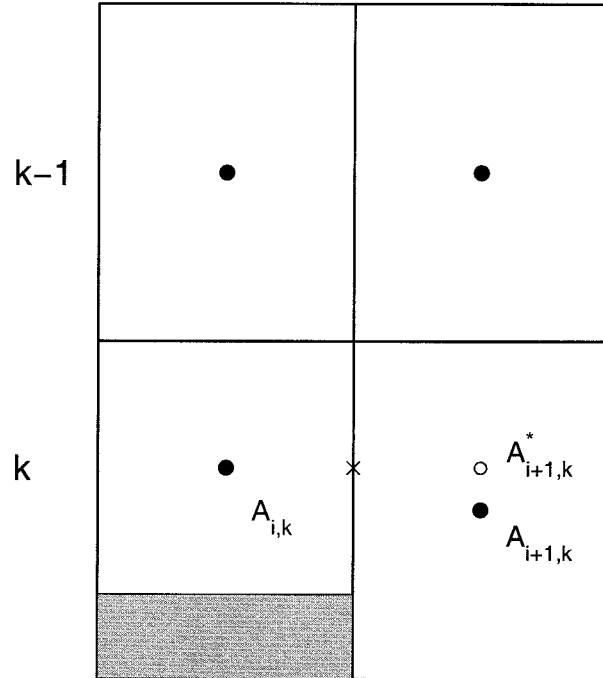nowski and Gnanadesikan (1998) for further details.

FIG. C1. A partial cell $A_{i,k}$ in the x–z plane with a regular cell $A_{i+1,k}$
to its right. The thickness of the partial cell is reduced by an amount
equal to the height of the shaded area. A solid circle denotes the
center of each cell. The open circle denotes the position at which the
values of the A-grid variables $A^*_{i+1,k}$ are calculated by vertical inter-
polation. The variables at $A_{i,k}$ and $A^*_{i+1,k}$ are either averaged or dif-
ferenced to provide estimates of velocity, flux, or pressure gradient
at the center of the intervening cell face (indicated by a $\times$).

Figure C1 shows the configuration of a partial cell,
centered at $A_{i,k}$, at the level k. Its thickness is reduced
by an amount equal to the height of the shaded area in
order to more accurately represent the real topography.
The cells at upper levels (the level $k - 1$ and above)
are full cells with no side boundaries adjoining partial
cells. Hence, all flux and conservation formulae are un-
changed for cells at the level $k - 1$ and above. The cell
at the right of the partial cell, centered at $A_{i+1,k}$, has
full thickness but has an adjoining side in common with
the partial cell. Both $A_{i,k}$ and $A_{i+1,k}$ need special treat-
ment. The following factors must be properly accounted
for in order to correctly implement partial cells.

1) The fluxes across cell boundaries affected by partial
cells must account for the reduced surface area of
the face. This is a simple matter of multiplying by
the appropriate cell height when calculating the
boundary flux.

2) The horizontal velocity component normal to a cell
face with reduced height must be interpolated to the
midlevel of the cell face (e.g., the position indicated
by $\times$ in Fig. C1) in order to maintain second order
accuracy in the advective fluxes. For our A-grid
model, the vertical interpolations are done at the A-
grid locations (to the position of the open circle in

Fig. C1), and then horizontal interpolation is used to determine the component of velocity normal to the intervening cell face.

3) The calculation of vertical velocity from the continuity equation must be based on the same interpolated horizontal velocity components as used in the calculation of advective fluxes. Note that the discretized continuity equation ensures the balance of volume fluxes across all surfaces of a control volume. The volume flux at the intervening cell face is the interpolated velocity at $\times$ multiplied by the area of that surface.

4) Horizontal diffusive fluxes must be based on differences between quantities that have been interpolated to the appropriate middepth level of the face. Once again, vertical interpolations are done on the A-grid, and then first differences are used to estimate the diffusive fluxes. If the quantity being interpolated is a simple linear function of depth, its horizontal diffusive flux is zero to within roundoff error in our model.

5) An estimate of the average pressure gradients over each cell volume is required. In the A-grid DieCAST model, the components of the pressure gradient normal to the cell faces are first determined at the middepth level of each cell face, and then these values are used to estimate the average over the cell volume by taking appropriate weighted averages. To determine the pressure gradient normal to a cell face, we first estimate the pressure at the appropriate level on each side of the face and then take the difference. To determine the pressure at the midlevel of the cell face, we first interpolate temperature and salinity to this level and use these to determine the in situ density. The density is then assumed to vary linearly between this level and the overlying level, and the hydrostatic equation is used to determine the change in pressure between these two levels. By using this approach, the horizontal pressure gradients are zero to within roundoff error, when T and S are linear functions of depth, even when using a nonlinear equation of state. Once the components of the pressure gradient normal to the cell faces are determined, a depth-weighted average [i.e., $A_i = (h_{i-1/2}A_{i-1/2} + h_{i+1/2}A_{i+1/2})/(2h_i)$] is used to estimate the gradient at the center of the cell. Note that the depth weighting makes the pressure gradient at a face have diminishing influence as the area of the face decreases. In the limit as the vertical extent of a cell face approaches either zero or the full cell thickness, we recover the standard formulae used to estimate the cell-centered pressure gradient on an A-grid.

6) Finally, it is possible for partial cells to be very thin, which can result in local numerical instabilities. One way to avoid this possibility would be to limit the minimum thickness of a partial cell such that the stability criterion is not violated. However, we prefer to avoid the resulting modification of the bottom topography. If, instead of having a very thin partial

cell, we had a cell that was slightly thicker than the normal cell depth, the stability problem would not occur. Unfortunately, this approach would introduce substantial additional complications, and hence we take a much simpler approach. We accomplish essentially the same effect by using an implicit scheme for the vertical momentum mixing and increasing the vertical viscosity between partial cells and the overlying cell when the partial cell is so thin that stability considerations might be a concern. In the present study, we have increased the vertical mixing at the top of partial cells when their thickness is less than 10 m. When this occurs, the vertical viscosity is increased to $(\Delta z)^2/\Delta t$, where Δz is the distance between the center of the partial cell and the center of the overlying cell. No increase in the vertical diffusivity for heat and salinity was needed or used in the present study.

REFERENCES

Adcroft, A., C. Hill, and J. Marshall, 1997: Representation of topography by shaved cells in a height coordinate ocean model. *Mon. Wea. Rev.,* **125,** 2293–2315.

Baines, P. G., 1982: On internal tide generation models. *Deep-Sea Res.,* **29,** 307–338.

Craig, P. D., 1987: Solutions for internal tidal generation over coastal topography. *J. Mar. Res.,* **45,** 83–105.

Cummins, P. F., and L.-Y. Oey, 1997: Simulation of barotropic and baroclinic tides off northern British Columbia. *J. Phys. Oceanogr.,* **27,** 762–781.

Davidson, F. J. M., R. J. Greatbatch, and A. D. Goulding, 1998: On the net cyclonic circulation in large stratified lakes. *J. Phys. Oceanogr.,* **28,** 527–534.

Dietrich, D. E., 1992: The Sadie ocean modeling system programmers guide and users' manual. Sandia National Laboratories SAND92-7386, 64 pp. [Available from Sandia National Laboratories, P.O. Box 5800, Albuquerque, NM 87185.]

——, and C. Lin, 1994: Numerical studies of eddy shedding in the Gulf of Mexico. *J. Geophys. Res.,* **99,** 7599–7615.

——, M. G. Marietta, and P. J. Roache, 1987: An ocean modeling system with turbulent boundary layers and topography: Numerical description. *Int. J. Numer. Methods Fluids,* **7,** 833–855.

Dukowicz, J. K., and R. D. Smith, 1994: Implicit free-surface method for the Bryan–Cox–Semtner ocean model. *J. Geophys. Res.,* **99,** 7991–8014.

Haney, R. L., 1991: On the pressure gradient force over steep topography in sigma coordinate ocean models. *J. Phys. Oceanogr.,* **21,** 610–619.

Holloway, P. E., 1996: A numerical model of internal tides with application to the Australia North West Shelf. *J. Phys. Oceanogr.,* **26,** 21–37.

——, and M. A. Merrifield, 1999: Internal tide generation by seamounts, ridges, and islands. *J. Geophys. Res.,* **104,** 25 937–25 951.

Killworth, P. D., D. Stainforth, D. J. Webb, and S. M. Paterson, 1991: The development of a free-surface of Bryan–Cox–Semtner ocean model. *J. Phys. Oceanogr.,* **21,** 1333–1348.

Mellor, G. L., T. Ezer, and L.-Y. Oey, 1994: On the pressure gradient conundrum of sigma coordinate ocean models. *J. Atmos. Oceanic Technol.,* **11,** 1126–1134.

Müller, P., and X. Liu, 2000: Scattering of internal waves at finite topography in two dimensions. Part I: Theory and case studies. *J. Phys. Oceanogr.,* **30,** 532–563.

Munk, W. H., 1997: Once again: Once again-tidal friction. *Progress in Oceanography,* Vol. 40, Pergamon, 7–35.

Pacanowski, R. C., and A. Gnanadesikan, 1998: Transient response in a z-level ocean model that resolves topography with partial cells. *Mon. Wea. Rev.,* **126,** 3248–3270.

Ray, R. D., and G. T. Mitchum, 1996: Surface manifestation of internal tides generated near Hawaii. *Geophys. Res. Lett.,* **23,** 2101–2104.

Rhines, P. B., 1975: Edge-, bottom- and Rossby Waves in a rotating stratified fluid. *Geophys. Fluid Dyn.,* **1,** 273–302.

Sandstrom, H., 1976: On topographic generation and coupling of internal waves. *Geophys. Fluid Dyn.,* **7,** 231–270.

——, and N. S. Oakey, 1995: Dissipation in internal tides and solitary waves. *J. Phys. Oceanogr.,* **25,** 604–614.

Sheng, J., 2001: Dynamics of a buoyancy-driven coastal jet: The Gaspé Current. *J. Phys. Oceanogr.*, in press.

——, D. G. Wright, R. J. Greatbatch, and D. E. Dietrich, 1998: CANDIE: A new version of the DieCAST ocean circulation model. *J. Atmos. Oceanic Technol.,* **15,** 1414–1432.

Smith, R. D., J. K. Dukowicz, and R. C. Malone, 1992: Parallel ocean circulation modeling. *Physics,* **60D,** 38–61.

Wright, D. G., and K. R. Thompson, 1983: Time-averaged forms of the nonlinear stress law. *J. Phys. Oceanogr.,* **13,** 341–345.

Xing, J., and A. M. Davies, 1996: Processes influencing the internal tide, its higher harmonics, and tidally induced mixing on the Malin–Hebrides Shelf. *Progress in Oceanography,* Vol. 38, Pergamon, 155–204.

——, and ——, 1998: Formulation of a three-dimensional shelf edge model and its application to internal tide generation. *Contin. Shelf Res.,* **18,** 405–440.